



Combination Cancer Therapy Very Important Paper



# Stanene-Based Nanosheets for $\beta$ -Elemene Delivery and Ultrasound-Mediated Combination Cancer Therapy

Wei Chen<sup>+</sup>, Chuang Liu<sup>+</sup>, Xiaoyuan Ji, John Joseph, Zhongmin Tang, Jiang Ouyang, Yufen Xiao, Na Kong, Nitin Joshi, Omid C. Farokhzad,\* Wei Tao,\* and Tian Xie\*

**Abstract:** Ultrasound (US)-mediated sonodynamic therapy (SDT) has emerged as a superior modality for cancer treatment owing to the non-invasiveness and high tissue-penetrating depth. However, developing biocompatible nanomaterial-based sonosensitizers with efficient SDT capability remains challenging. Here, we employed a liquid-phase exfoliation strategy to obtain a new type of two-dimensional (2D) stanene-based nanosheets (SnNSs) with a band gap of 2.3 eV, which is narrower than those of the most extensively studied nanosonosensitizers, allowing a more efficient US-triggered separation of electron ( $e^-$ )-hole ( $h^+$ ) pairs for reactive oxygen species (ROS) generation. In addition, we discovered that such SnNSs could also serve as robust near-infrared (NIR)-mediated photothermal therapy (PTT) agents owing to their efficient photothermal conversion, and serve as nanocarriers for anticancer drug delivery owing to the inherent 2D layered structure. This study not only presents general nanoplatforms for SDT-enhanced combination cancer therapy, but also highlights the utility of 2D SnNSs to the field of nanomedicine.

## Introduction

Despite tremendous progress in cancer therapies, cancer remains one of the most notorious diseases worldwide. Photodynamic therapy (PDT) which takes advantage of the cytotoxic reactive oxygen species (ROS) generated by light-activated photosensitizers to kill cancer cells has shown great

promise for cancer therapy in clinical settings.<sup>[1–3]</sup> Yet, PDT suffers from low tissue-penetrating depth (on the order of millimeters) and inherent phototoxicity from the photosensitizers, thereby hindering the treatment efficacy for deep-seated tumors and producing undesirable side effects.<sup>[4]</sup> To address these shortcomings, ultrasound (US)-mediated sonodynamic therapy (SDT) has recently emerged as a powerful modality for disease treatments owing to the non-invasiveness, spatiotemporal controllability, and most importantly, high tissue-penetrating depth (on the order of centimeters).<sup>[5–7]</sup> Consequently, compared with PDT, SDT has become a superior noninvasive modality for disease treatments. Similar to PDT, the execution of SDT relies on the efficient separation of electron ( $e^-$ )-hole ( $h^+$ ) pairs within the US-activated sonosensitizers; the  $e^-$  and  $h^+$ , and the energy released from the activated sonosensitizers could further react with the surrounding  $O_2$  and  $H_2O$  molecules to generate cytotoxic ROS (e.g.,  $^1O_2$ , and  $\cdot OH$ ).<sup>[8]</sup> Given this paradigm, the synthesis of desirable sonosensitizers that can efficiently generate ROS by the US trigger plays a pivotal role in executing SDT.

The advantageous US-triggered generation of ROS for SDT was originally showcased with organic small molecule sonosensitizers, such as porphyrins, their derivatives, and others.<sup>[5,9,10]</sup> However, their long-lasting skin sensitivity, low chemical stability, poor tumor accumulation, and high dose-dependent toxicity have hindered their further applications in clinical settings. Additionally, the hydrophobic nature of most of these small molecules makes them easily aggregate in the physiological environment, thereby reducing their bioavailability and ROS generation efficiency.<sup>[7]</sup> To solve the unmet needs the past years have seen a focus on the synthesis of biocompatible inorganic nanomaterial-based sonosensitizers such as titanium dioxide ( $TiO_2$ ), zinc oxide (ZnO) nanomaterials, and their nanocomposites.<sup>[11–13]</sup> These studies have substantially increased the chemical stability, biocompatibility, and desirable tumor accumulation for SDT. However, challenges remain in the US-triggered ROS generation efficiency since  $TiO_2$  and ZnO are known to have the wide band gaps (3.2 eV and 3.4 eV, respectively) and fast combinations of excited electrons and holes,<sup>[14]</sup> which may hinder their further biomedical applications. Consequently, the synthesis of biocompatible sonosensitizers with superior ROS generation efficiency is urgently needed for SDT.

Inspired by the unprecedented success of graphene, two-dimensional (2D) monoelemental materials (Xenes) and their derivatives have received ever-increasing attention during the past years.<sup>[15]</sup> These have been seen in the elements

[\*] Dr. X. Ji, Prof. Dr. T. Xie  
College of Pharmacy, School of Medicine, Hangzhou Normal University  
Hangzhou, Zhejiang, 311121 (China)  
E-mail: tianxie@hznu.edu.cn

Dr. W. Chen,<sup>[†]</sup> C. Liu,<sup>[†]</sup> Dr. X. Ji, Dr. J. Joseph, Dr. Z. Tang,  
Dr. J. Ouyang, Y. Xiao, Dr. N. Kong, Prof. Dr. N. Joshi,  
Prof. Dr. O. C. Farokhzad, Prof. Dr. W. Tao  
Center for Nanomedicine and Department of Anesthesiology,  
Brigham and Women's Hospital, Harvard Medical School  
Boston, MA 02115 (USA)  
E-mail: ofarokhzad@bwh.harvard.edu  
wtao@bwh.harvard.edu

Prof. Dr. N. Joshi  
Department of Chemical Engineering and Koch Institute for  
Integrative Cancer Research, Massachusetts Institute of Technology  
Cambridge, MA 02139 (USA)

[†] These authors contributed equally to this work.

Supporting information and the ORCID identification number(s) for the author(s) of this article can be found under:  
 <https://doi.org/10.1002/anie.202016330>.

of group IIIA (B: borophene; Ga: gallenene),<sup>[16,17]</sup> group IVA (Si: silicene; Ge: germanene),<sup>[18–21]</sup> group VA (P: phosphorene; As: arsenene; Sb: antimonene; Bi: bismuthene),<sup>[22–26]</sup> and group VIA (Se: selenene; Te: tellurene).<sup>[27,28]</sup> Due to the unique structures and physicochemical properties, Xenes have a variety of promising applications, including catalysis, energy storage, electronics, and biomedicine.<sup>[29]</sup> Notably, the recently discovered 2D stanene (Sn in group IVA) has fascinated scientists owing to its unique electronic structures, excellent quantum effects, thermoelectric properties, and superconductivity.<sup>[30,31]</sup> All these promising properties indicate that 2D stanene and its derivatives could serve as new 2D materials for a variety of applications. More importantly, since the band gap of stanene oxide is 2.5 eV,<sup>[32,33]</sup> narrower than those of TiO<sub>2</sub> (3.2 eV) and ZnO (3.4 eV) conventional nano-sonosensitizers,<sup>[34]</sup> we envision that such 2D stanene-based nanostructures could potentially serve as advantageous sonosensitizers for SDT. Despite the superior physicochemical advantages of 2D stanene, to the best of our knowledge, the experimental efforts and applications of 2D stanene and its derivatives remain largely unexplored and are still in their infancy, especially in nanomedicine for cancer therapies.

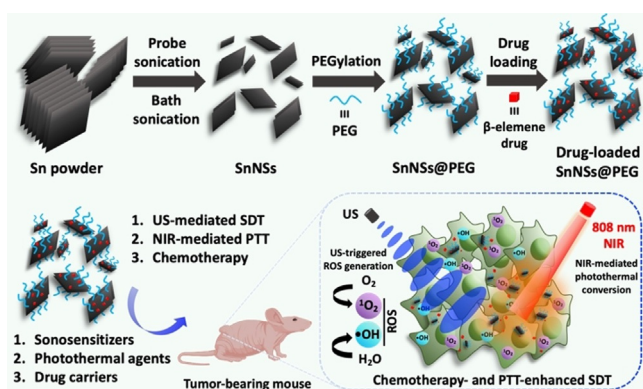
Originally, 2D stanene was primarily fabricated by the epitaxial growth on various substrates by which the morphology and electronic properties of 2D stanene could be well-controlled.<sup>[30,31,35]</sup> Yet, the strong adhesion of the 2D stanene on the corresponding substrates undermined the practical usage of the 2D stanene nanomaterials alone. In efforts to set the stage for biomedical applications, here, for the first time we employed a liquid-phase exfoliation strategy to the large-scale synthesis of 2D stanene-based nanosheets (SnNSs), and applied such SnNSs as a new type of sonosensitizer to achieve efficient US-triggered ROS (<sup>1</sup>O<sub>2</sub> and ·OH) generation (Scheme 1). In addition, we discovered that such black 2D SnNSs could serve as robust photothermal agents for near-infrared (NIR)-mediated photothermal therapy (PTT) owing to their strong NIR absorption and efficient photothermal conversion. The photothermal conversion efficiency of SnNSs (37.9%) is much higher than many other nanomaterial-based photothermal agents, such as Au nanorods,<sup>[36]</sup> graphene

oxide,<sup>[37]</sup> MoS<sub>2</sub> nanocrystals,<sup>[38]</sup> and black phosphorus,<sup>[39,40]</sup> rendering SnNSs excellent photothermal agents for PTT. Moreover, the inherent 2D layered structure with a high surface-to-volume ratio enables SnNSs to function as drug carriers for anticancer drug delivery. In summary, this study not only provides a robust strategy for large-scale synthesis of 2D stanene-based nanosheets as sonosensitizers for SDT but also creates a general nanoplatform for tri-modal combination cancer therapies. We believe that, owing to the unique band gap and the electronic structure, these 2D SnNSs may hold great potentials to serve as photocatalysts and thus highlight the significance of their applications in the field of catalysis and energy.

## Results and Discussion

**Synthesis and Characterization of Ultrasound-Activatable SnNSs.** SnNSs were obtained by a liquid-phase exfoliation strategy through sonicating 10 μm Sn powder in isopropanol by an ultrasound probe and water bath sonication. The morphology of the obtained SnNSs was characterized by transmission electron microscope (TEM) and atomic force microscope (AFM). The TEM and AFM images showed that the lateral size and thickness of the observed SnNSs were approximately 100–200 nm and 4.4 nm, respectively (Figure 1 a–c). The chemical composition and crystal structure of SnNSs were determined by X-ray photoelectron spectroscopy (XPS), scanning electron microscope (SEM)/energy dispersive X-ray spectrometer (EDS) elemental mapping, and X-ray diffraction (XRD) pattern. The peaks at 486 eV, 495 eV, and 531 eV in the XPS survey spectrum (Figure S1, SI) of SnNSs could be assigned to Sn 2d and O 1s. Interestingly, both SnO (495.2 eV: 3d<sub>3/2</sub> and 486.8 eV: 3d<sub>5/2</sub>) and Sn (493.3 eV: 3d<sub>3/2</sub> and 484.8 eV: 3d<sub>5/2</sub>) were found in the XPS spectrum with a ratio of SnO/Sn = 8.2/1.0 (Figure 1 d). The oxidation of SnNSs likely resulted from the existence of stanene oxide (SnO), which was attributed to the oxidation by air during the exfoliation process.<sup>[18]</sup> SEM/EDS elemental mapping images (Figure 1 e) showed the homogeneous distribution of Sn and O on the entire SnNSs, further supporting the existence of Sn and O elements in the structure of SnNSs. XRD pattern of SnNSs (Figure 1 f) displayed the crystalline structure of tetragonal β-Sn (ICDD No. 04-0673).<sup>[41]</sup> However, the crystalline structure of SnO was not found in the XRD pattern, suggesting the existence of amorphous structure of SnO in the SnNSs.

To enhance the colloidal stability of SnNSs in the physiological environments, we coated the surface of SnNSs with DSPE-PEG (1,2-distearoyl-*sn*-glycero-3-phosphoethanolamine-*N*-[methoxy(polyethylene glycol)]), and the resulting nanomaterials were designated as SnNSs@PEG. The successful PEG coating was confirmed by Fourier transform infrared (FTIR), zeta potential value measurement, and thermogravimetric analysis (TGA). The appearance of absorption bands at 2892, 1745, 1460 and 1335, and 1103 cm<sup>-1</sup> in the FTIR spectrum of SnNSs@PEG corresponded to C–H stretching, C=O stretching, C–H bending, and C–O stretching, respectively, demonstrating the successful PEG modification



**Scheme 1.** Schematic illustration of the preparation of polyethylene glycol (PEG)-functionalized two-dimensional (2D) stanene-based nanosheets (SnNSs@PEG) by a liquid-phase exfoliation strategy and their applications for chemotherapy- and photothermal therapy (PTT)-enhanced sonodynamic therapy (SDT).

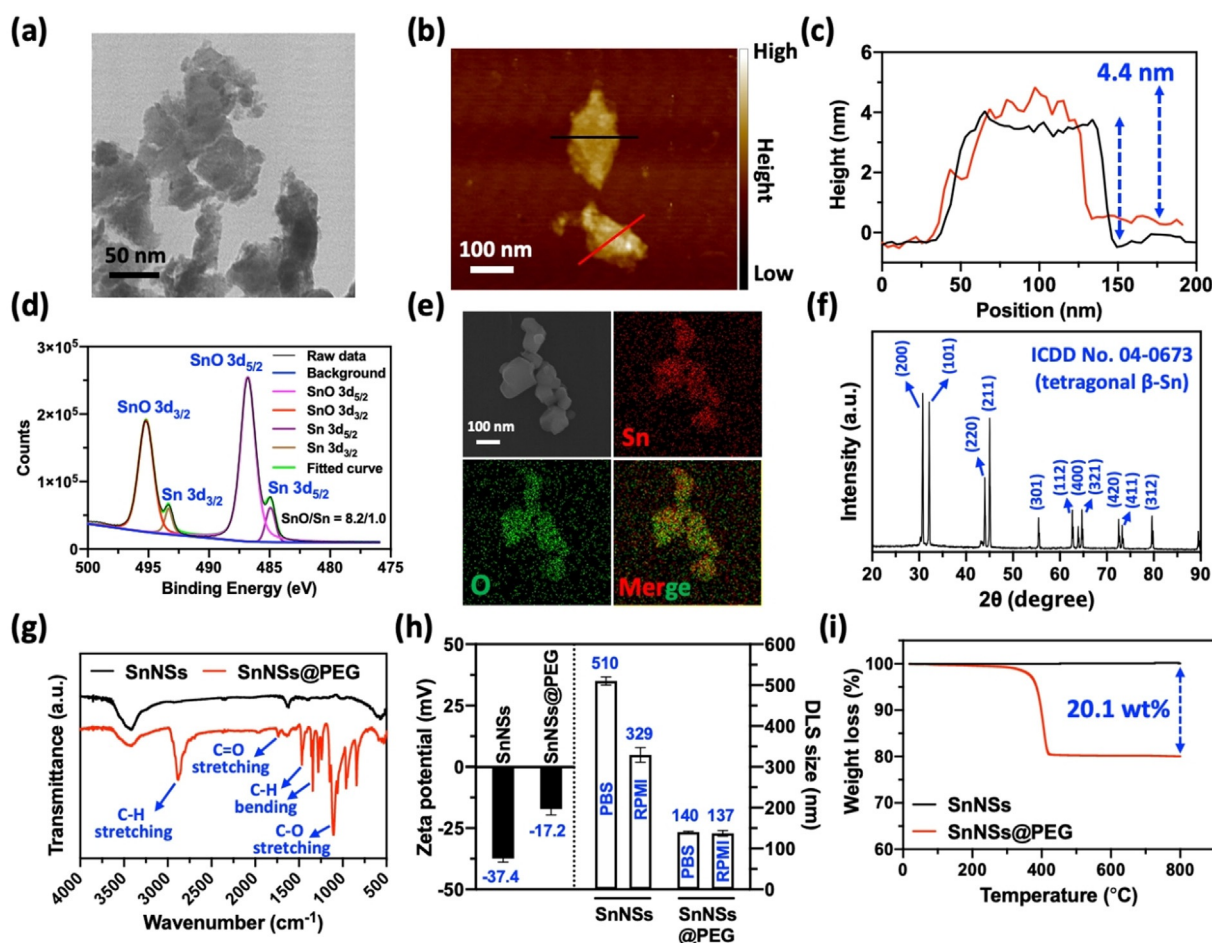


**Figure 1.** Characterization of SnNSs and SnNSs@PEG. a) TEM image, b) AFM image, and c) the corresponding height profile of SnNSs. d) XPS spectrum, e) SEM/EDS elemental mapping images, and f) XRD pattern of SnNSs. g) FTIR spectra, h) zeta potential values and DLS sizes ( $n = 3$ ), and i) TGA of SnNSs and SnNSs@PEG.

on the SnNSs surface (Figure 1g). Additionally, the zeta potential value of SnNSs@PEG measured in deionized water at room temperature was  $-17.2 \pm 2.4$  mV, less negative than that of SnNSs ( $-37.4 \pm 1.5$  mV), showing that DSPE-PEG was coated on the surface of SnNSs (Figure 1h). Additionally, the weight loss difference between SnNSs and SnNSs@PEG after heating to  $800^\circ\text{C}$  was 20.1 wt% (Figure 1i), suggesting an efficient PEG coating on SnNSs surface. Dynamic light scattering (DLS) analysis showed that the sizes of SnNSs@PEG were  $140 \pm 2$  nm and  $137 \pm 7$  nm in phosphate-buffered saline (PBS) solution and RPMI-1640 cell medium with 10% fetal bovine serum, respectively (Figure 1h; Figure S2b, SI). In contrast, the DLS sizes of SnNSs were  $510 \pm 10$  nm and  $329 \pm 18$  nm in those two buffer solutions, respectively (Figure 1h; Figure S2a, SI). The results demonstrated that the PEG coating on the surface of SnNSs substantially enhanced the colloidal stability of SnNSs in the physiological environments and thus was advantageous for further biological studies.

**Sonodynamic Performance of SnNSs@PEG.** To explore the potential of SnNSs@PEG as sonosensitizers for sonodynamic therapy (SDT), we employed 1,3-diphenylisobenzofuran (DPBF) and 3,3',5,5'-tetramethylbenzidine (TMB) as

singlet oxygen and hydroxyl radical probes to monitor the generation of  $^1\text{O}_2$  and  $\cdot\text{OH}$  by US-triggered SnNSs@PEG.<sup>[8,42–45]</sup> The US-triggered generation of  $^1\text{O}_2$  was carried out by exposing the solution containing a mixture of SnNSs@PEG and DPBF to an ultrasound probe (1 MHz,  $1\text{ W cm}^{-2}$ , 50% duty cycle) (Figure 2a). The characteristic peak of DPBF at 410 nm in the UV/Vis spectra gradually decreased with increasing US exposure time (Figure 2b). The results demonstrated that  $^1\text{O}_2$  generated by US-triggered SnNSs@PEG reacted with DPBF and generated colorless 1,2-dibenzoylbenzene over time (Figure 2a). Comparatively, negligible absorbance decreases at 410 nm were observed for other control groups (DPBF, DPBF + US, and DPBF + SnNSs@PEG) (Figure 2c; Figure S3, SI). Additionally, we used TMB to detect the generation of  $\cdot\text{OH}$  by US-triggered SnNSs@PEG with the same US parameters (Figure 2d). The absorbance peaks of the oxidized TMB at 654 nm in the UV/Vis spectra gradually increased with increasing US exposure time (Figure 2e). The results proved that  $\cdot\text{OH}$  generated by US-triggered SnNSs@PEG reacted with TMB and produced blue 3,3',5,5'-tetramethylbenzidine diimine over time (Figure 2d). In contrast, no prominent absorbance peaks at 654 nm were observed for other control groups (TMB, TMB

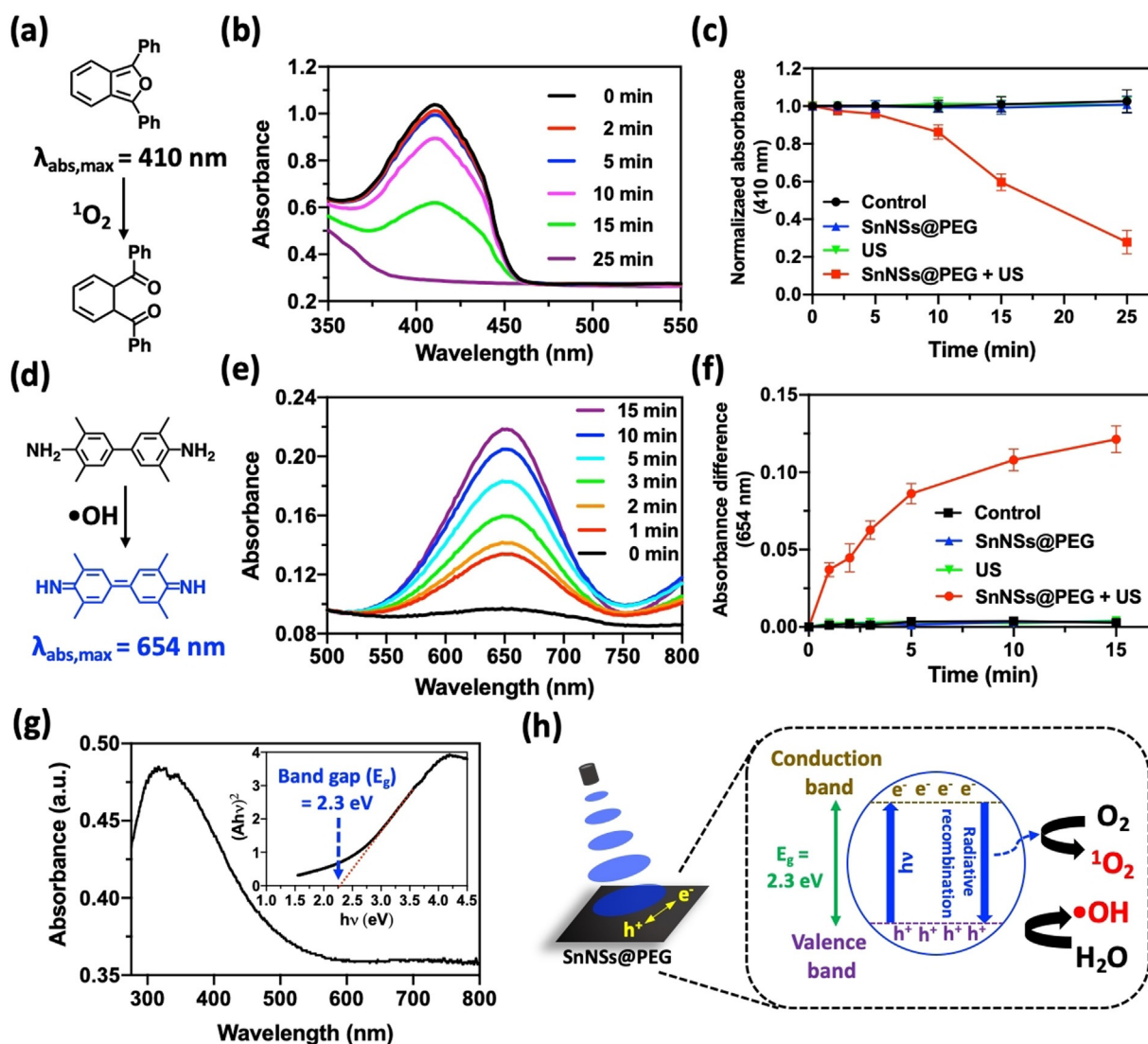


**Figure 2.** Sonodynamic performance of SnNSs@PEG. a,b) Time-dependent oxidation of DPBF showing  $^1\text{O}_2$  generation by US-triggered SnNSs@PEG. c) Comparison of DPBF oxidation by SnNSs@PEG + US, SnNSs@PEG, US only, and control groups ( $n=3$ ). The concentration of SnNSs@PEG is  $200\ \mu\text{g mL}^{-1}$ . d,e) Time-dependent oxidation of TMB showing  $\cdot\text{OH}$  generation by US-triggered SnNSs@PEG. The concentration of SnNSs@PEG is  $300\ \mu\text{g mL}^{-1}$ . f) Comparison of TMB oxidation by SnNSs@PEG + US, SnNSs@PEG, US only, and control groups ( $n=3$ ). g) UV/Vis/NIR diffuse reflectance spectra of SnNSs. Inset shows the corresponding optical band gap ( $E_g$ ) of SnNSs calculated by Kubelka-Munk equation. h) Proposed mechanism of sonodynamic performance of US-triggered SnNSs@PEG.

+ US, and TMB + SnNSs@PEG (Figure 2f; Figure S4, SI). Collectively, the  $^1\text{O}_2$  and  $\cdot\text{OH}$  generation by US-triggered SnNSs@PEG demonstrated that SnNSs@PEG, with the desirable sonodynamic performance, could serve as potential sonosensitizers for SDT.

To study the mechanism of sonodynamic performance of SnNSs, the optical absorbance spectrum of solid SnNSs was measured and a Tauc plot of the Kubelka–Munk (KM) function was plotted to calculate the optical band gap ( $E_g$ ) of SnNSs. The  $E_g$  of SnNSs was measured to be 2.3 eV (Figure 2g), which could be attributed to the existence of stanene oxide (SnO) semiconductor in the SnNSs and is consistent with the previous reports.<sup>[32,33]</sup> The band gap is related to the required minimum energy to achieve electron excitation. Therefore, the narrower band gap could facilitate the US-

triggered separation of the electron ( $e^-$ )-hole ( $h^+$ ) pairs followed by the ROS generation.<sup>[43]</sup> The mechanism of US-triggered generation of ROS by SnNSs is summarized in Figure 2h. Under the US exposure, the electrons in the valence band of SnNSs received energy and were excited to the conduction band to form electron-hole pairs, followed by the energy released from the US-activated SnNSs during the radiative recombination process. The released energy and holes were captured by the surrounding  $\text{O}_2$  and  $\text{H}_2\text{O}$  molecules to generate  $^1\text{O}_2$  and  $\cdot\text{OH}$  ROS, respectively.<sup>[8,46]</sup> Compared with the band gap of other nano-sonosensitizers in the previous studies, e.g.,  $\text{TiO}_2$  ( $E_g$ : 3.2 eV),<sup>[47,48]</sup>  $\text{TiH}_{1.924}$  ( $E_g$ : 2.7 eV),<sup>[49]</sup> and  $\text{ZnO}$  ( $E_g$ : 3.4 eV),<sup>[34]</sup> the narrower  $E_g$  of SnNSs in this study suggested a more efficient US-activated separation of electron-hole pairs for ROS generation, and thus was

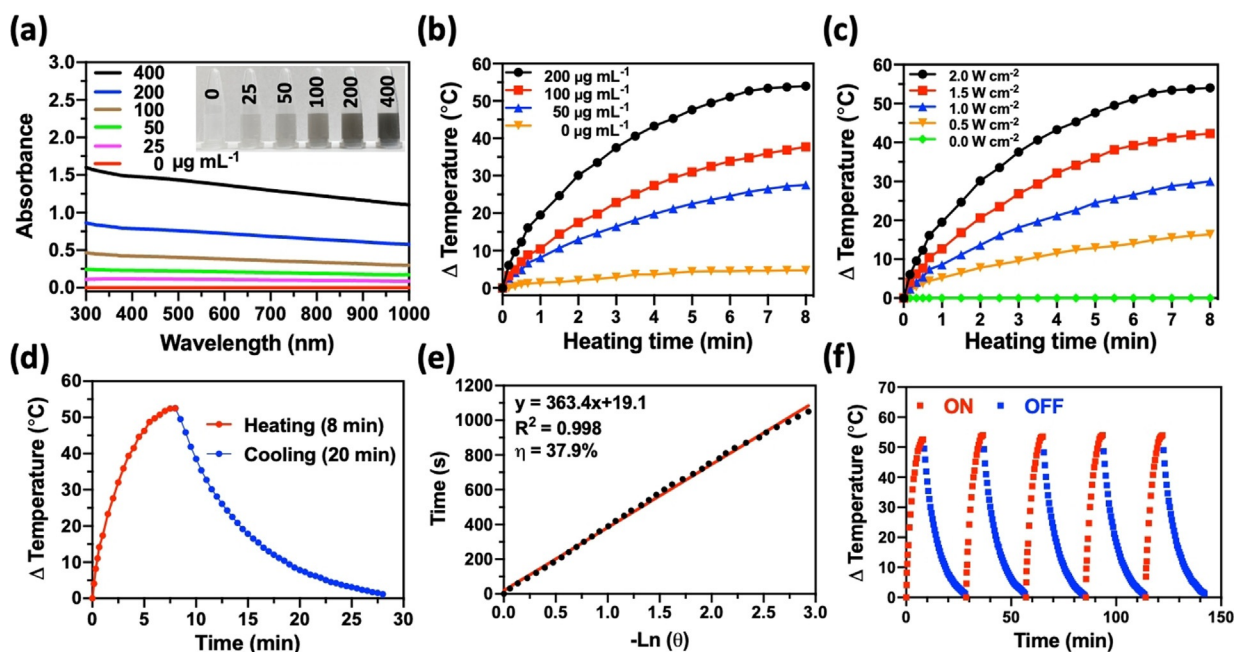


**Figure 3.** Photothermal performance of SnNSs@PEG. a) UV/Vis/NIR absorption spectra of SnNSs@PEG at various concentrations. Inset shows the photo of SnNSs@PEG dispersed in H<sub>2</sub>O at various concentrations. b) Concentration-, and c) NIR power density-dependent temperature-increase profiles of water containing SnNSs@PEG irradiated by an 808 nm NIR laser. The power density (b) and SnNSs@PEG concentration (c) are 2.0 W cm<sup>-2</sup>, and 200 µg mL<sup>-1</sup>, respectively. d) Photothermal heating and cooling profile of SnNSs@PEG. The SnNSs@PEG concentration and power density of the NIR laser were 200 µg mL<sup>-1</sup>, and 2.0 W cm<sup>-2</sup>, respectively. e) Linear fitting curve of time and  $-\ln(\theta)$  acquired from the cooling period of (d). f) Heating and cooling profiles for 5 repeated ON/OFF cycles of 808 nm laser irradiation. The SnNSs@PEG concentration and power density of the NIR laser were 200 µg mL<sup>-1</sup>, and 2.0 W cm<sup>-2</sup>, respectively.

more favorable for US-mediated SDT for cancer treatments.<sup>[43,49]</sup>

**Photothermal Performance of SnNSs@PEG.** The black SnNSs@PEG prompted us to further explore the photothermal performance of SnNSs@PEG. The UV/Vis/NIR absorption spectra of SnNSs@PEG showed a broad and strong absorption spanning from UV to NIR regions (Figure 3a), in which light would have much deeper tissue penetration depth in comparison to those in the UV and visible light. Given this paradigm, we envision that SnNSs@PEG could serve as photothermal agents for effective NIR-mediated PTT. The NIR-mediated photothermal performance was studied by exposing the water solution containing SnNSs@PEG to an 808 nm NIR laser. The photothermal heating profiles displayed strong dependence between temperature increase and (i) SnNSs@PEG concentration (Figure 3b), and (ii) power density of NIR laser (Figure 3c), with the highest temperature increase up to 52.5 °C at the concentration and the power density of 200 µg mL<sup>-1</sup> and 2 W cm<sup>-2</sup>, respectively (Figure S5, SI). In contrast, minimal temperature increase (4 °C) was observed when water was irradiated by NIR for 8 min. To determine the photothermal efficacy of SnNSs@PEG, the photothermal conversion efficiency (PTCE,  $\eta$ ), calculated according to the previous method (SI), was determined to be 37.9% (Figure 3de; Figure S6, SI), which is much higher than the majority of photothermal agents including Au nanorods (21%),<sup>[50]</sup> Cu<sub>2-x</sub>Se nanocrystals (22%),<sup>[50]</sup> MoS<sub>2</sub> nanosheet (24%),<sup>[38]</sup> black phosphorous quantum dots (28.4%),<sup>[39]</sup> and Bi<sub>2</sub>S<sub>3</sub>

nanorods (28.1%).<sup>[51]</sup> The remarkable  $\eta$  makes SnNSs@PEG superior photothermal agents for NIR-mediated cancer therapy. To investigate the photothermal stability of SnNSs@PEG, an aqueous solution containing SnNSs@PEG was repeatedly exposed to an 808 nm NIR laser for 8 min (ON) followed by naturally cooling to room temperature (OFF). As shown in Figure 2f and Figure S7a (SI), SnNSs@PEG exhibited stable photothermal performance for 5 ON/OFF cycles, rendering SnNSs@PEG robust photothermal agents for PTT. The photothermal stability of SnNSs@PEG was further confirmed by the UV/Vis/NIR spectra (Figure S7b, SI); negligible absorbance change across the entire spectra was observed after 5 cycles of ON/OFF NIR laser treatment.

**Delivery of  $\beta$ -Elemene Anticancer Drug by SnNSs@PEG.** Considering the similarity of the 2D layered structure of SnNSs@PEG to other 2D drug nanocarriers, such as graphene, black phosphorous, and MoS<sub>2</sub>,<sup>[52]</sup> we further investigated the potential of using SnNSs@PEG for anticancer drug delivery. A hydrophobic anticancer model drug,  $\beta$ -elemene, was loaded on SnNSs@PEG by soaking SnNSs@PEG in different concentrations of  $\beta$ -elemene solution for 24 h followed by washing with PBS (Figure S8a, SI). The loading of  $\beta$ -elemene is discussed in more details in SI (Figure S8 and S9). Moreover, the NIR-responsive release of  $\beta$ -elemene was studied.  $\beta$ -elemene-loaded SnNSs@PEG was exposed to 10 min of NIR irradiation at 2 h, 4 h, and 6 h after the release starting point (Figure S8d, SI). The burst releases of  $\beta$ -elemene from SnNSs@PEG were observed; the release

efficiency increases of 15.7%, and 8.1% were measured after 10 min of NIR irradiation at 2 h and 4 h, respectively. The results showed that the NIR-mediated local hyperthermia by SnNSs@PEG could not only execute PTT but also function as on/off stimulus to control the release of  $\beta$ -elemene small molecule anticancer drugs from SnNSs@PEG since a high concentration of drug could be delivered to their surroundings in a short period.<sup>[22,53]</sup> Additionally, the release finally leveled off at 6 h ( $87.6 \pm 0.8\%$ ), much earlier than that without NIR irradiation, suggesting the NIR-responsive SnNSs@PEG could efficiently release their payload in a spatiotemporally controlled manner.

**In Vitro Studies of Cytotoxicity and Cellular Uptake of SnNSs@PEG.** The successful demonstration of US-triggered ROS generation, NIR-mediated photothermal performance, and anticancer drug delivery by SnNSs@PEG prompted us to explore the potential of the multifunctional stanene-based nanoplatforms for in vitro therapeutic studies on cancer cells. To evaluate the potential of SnNSs@PEG for further biological applications, we first investigated the biocompatibility and cellular uptake of SnNSs@PEG. No cytotoxicity of SnNSs@PEG was observed for normal cells including HEK293 (human embryonic kidney cells), THLE-3 (human liver epithelial cells), and cancer cells including H1299 (a human non-small cell lung carcinoma cell line), and HeLa (a human cervical cell line) even at a very high concentration ( $200 \mu\text{g mL}^{-1}$ ) for 24 h (Figure 4a) or 60 h for H1299 cells (Figure S10, SI), rendering SnNSs@PEG biocompatible nanomaterials for multimodal synergistic cancer therapy. We next analyzed the cellular uptake of SnNSs@PEG using

Cy5-labeled SnNSs@PEG (SnNSs@PEG-Cy5) by a confocal laser scanning microscope (CLSM). The cellular uptake of SnNSs@PEG-Cy5 by H1299 cancer cells was correlated with the lengths of incubation time; a stronger red fluorescence intensity around the nuclei (blue fluorescence) was detected with longer incubation time (Figure 4b; Figure S11, SI), implying that more uptake of SnNSs@PEG-Cy5 by H1299 cells was observed. It is worth mentioning that the uptake could even be observed when the incubation time was only 2 h, suggesting that the efficient uptake was advantageous for further therapeutic studies.

**In Vitro Chemotherapy- and PTT-enhanced SDT.** In vitro SDT performance of SnNSs@PEG was subsequently studied to demonstrate the therapeutic efficacy of SnNSs@PEG. H1299 cells were treated by various concentrations of SnNSs@PEG followed by the US irradiation for 3 min (1 min per cycle, 3 cycles). The results showed that no cell viability decrease of the US only group was observed (Figure 4c; Figure S12a, SI), indicating the US exposure was harmless to cells and is a biocompatible treatment modality for cancer therapy.<sup>[54–58]</sup> In contrast, the viabilities of H1299 cells were 85%, 72%, 53%, and 28% when the SnNSs@PEG concentrations were 25, 50, 100, and  $200 \mu\text{g mL}^{-1}$ , respectively (Figure 4c; Figure S12a, SI). The viabilities of H1299 significantly decreased with increasing SnNSs@PEG concentrations, indicating the effective concentration-dependent SDT for SnNSs@PEG-treated H1299 cells. To investigate the intracellular mechanism of US-mediated cell killing by SnNSs@PEG, we used 2,7-dichlorofluorescein diacetate ( $\text{H}_2\text{DCF-DA}$ ) staining assay to monitor the intracellular

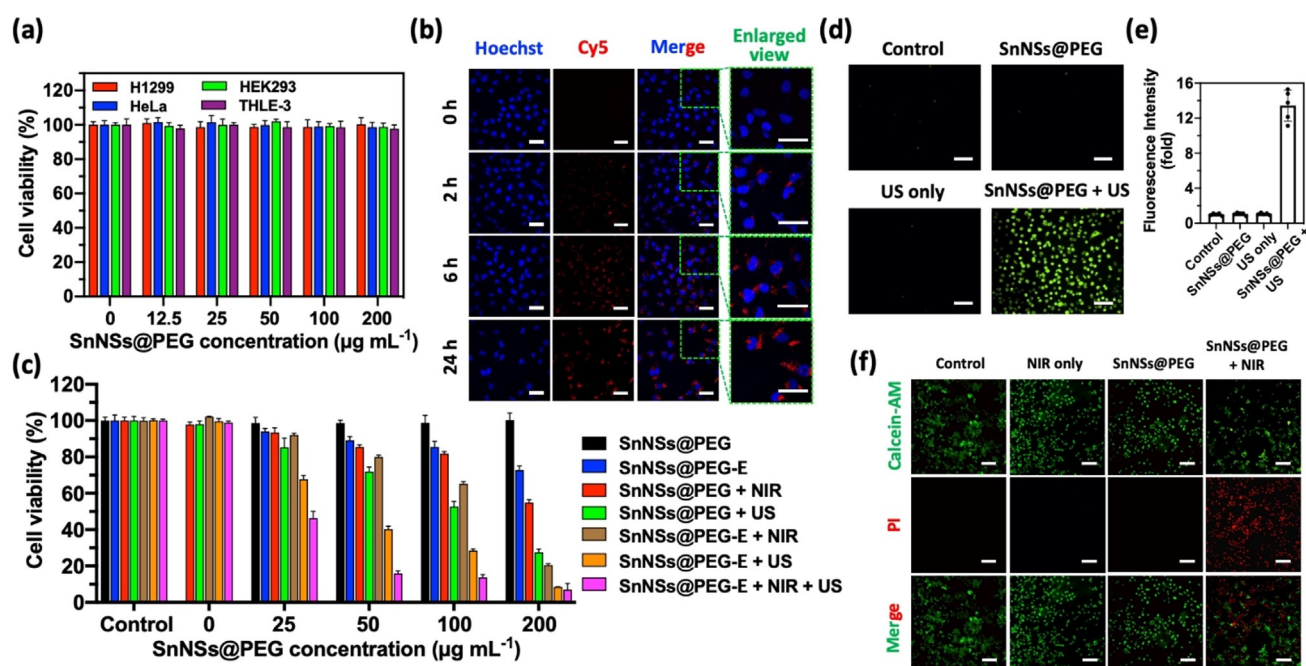


**Figure 4.** In vitro chemotherapy- and PTT-enhanced SDT. a) Cytotoxicity of SnNSs@PEG against different cells after 24 h of incubation. Cell viability was determined by an AlamarBlue assay and normalized to the control without SnNSs@PEG treatment ( $n=5$ ). b) Confocal laser scanning microscope (CLSM) images of the uptake of Cy5-labeled SnNSs@PEG by H1299 cells. Scale bars are  $20 \mu\text{m}$ . c) Viability of H1299 cells after various treatments ( $n=5$ ). d) Fluorescence microscope images and e) the corresponding fluorescence intensity of  $\text{H}_2\text{DCF-DA}$ -stained H1299 cells after various treatments. Scale bar is  $100 \mu\text{m}$  ( $n=5$ ). f) Fluorescence microscope images of Calcein-AM (green, live cells) and PI (red, dead cells) co-stained H1299 cells after various treatments. Scale bars are  $200 \mu\text{m}$ .

ROS generation; green fluorescence represents the intracellular ROS production.<sup>[59]</sup> Fluorescence microscope images of control groups (without treatment, SnNSs@PEG, and US only) showed minimal fluorescence intensity (Figure 4de), indicating negligible ROS was generated. In contrast, strong green fluorescence in the H1299 cells was observed when cells were treated by SnNSs@PEG followed by the US exposure; 13 times higher than those of other control groups (Figure 4e). Consequently, the data revealed that the US-triggered SnNSs@PEG sonosensitizers efficiently generated intracellular ROS and led to the cell death by SDT.

Since SnNSs@PEG exhibited excellent photothermal conversion efficiency, we further investigated the in vitro NIR-mediated therapeutic effect of SnNSs@PEG. H1299 cells were incubated with SnNSs@PEG at various concentrations for 24 h followed by NIR irradiation (808 nm,  $1 \text{ W cm}^{-2}$ ) for 10 min. Like US-mediated cell killing, the cell viability decreased with increasing SnNSs@PEG concentration as the cell viability decreased to 55% at a concentration of  $200 \mu\text{g mL}^{-1}$  (Figure 4c; Figure S12b, SI). The cell killing primarily resulted from the NIR-mediated temperature increases of the cell solution;  $25.0^\circ\text{C}$  of temperature increase was measured after 10 min of NIR irradiation at the SnNSs@PEG concentration of  $200 \mu\text{g mL}^{-1}$  (Figure S13, SI). The live/dead cells co-staining assay further confirmed the PTT therapeutic effect of SnNSs@PEG against H1299 (Figure 4f). Compared with other control groups (Control, NIR only, and SnNSs@PEG; green for live cells), only when cells were treated by SnNSs@PEG followed by NIR irradiation shows the existence of dead cells (red). Collectively, the findings further demonstrated that the biocompatible SnNSs@PEG possessed remarkable therapeutic effects through NIR-mediated PTT. To investigate the chemotherapy-enhanced SDT and PTT performance of SnNSs@PEG, the in vitro dual combination therapies were then studied. H1299 cells were treated by  $\beta$ -elemene-loaded SnNSs@PEG (SnNSs@PEG-E) for 24 h followed by US (3 min) or NIR (10 min) irradiation; i.e., SnNSs@PEG-E + US and SnNSs@PEG-E + NIR. Compared with SDT and PTT alone, the chemotherapy-enhanced SDT and chemotherapy-enhanced PTT substantially decreased the cell viabilities for all of the SnNSs@PEG-E concentrations tested (Figure 4c; Figure S12cd, SI). It was found that the cell viability decreased to only 8% and 21% after the SnNSs@PEG-E + US, and SnNSs@PEG-E + NIR treatment at  $200 \mu\text{g mL}^{-1}$ , respectively. The results indicated that chemotherapy could effectively enhance the SDT and PTT therapeutic efficacy of SnNSs@PEG.

To maximize the SDT performance of SnNSs@PEG-E, we employed the chemotherapy- and PTT-enhanced SDT tri-modal combination therapy against H1299 cancer cells. Excitingly, the cell viability was only 6% after the treatment by SnNSs@PEG-E ( $200 \mu\text{g mL}^{-1}$ ) followed by the NIR and US irradiation (Figure 4c; Figure S12e, SI). It is worth mentioning that when cells were treated by the lower SnNSs@PEG-E concentrations, superior therapeutic efficacy was still measured; cell viabilities decreased to only 16% ( $50 \mu\text{g mL}^{-1}$ ) and 13% ( $100 \mu\text{g mL}^{-1}$ ). Compared with the chemotherapy-enhanced SDT and chemotherapy-enhanced

PTT (40% and 28% for SnNSs@PEG-E + US; 79% and 65% for SnNSs@PEG-E + PTT at 50 and  $100 \mu\text{g mL}^{-1}$ , respectively), the significant cell viabilities decrease demonstrated that SnNSs@PEG-E could serve as effective sonosensitizers, photothermal agents, and anticancer drug carriers since the tri-modal combination therapy showed excellent anticancer performance and was more superior than all single (Figure 4c; Figure S12abf, SI) and dual combinations (Figure 4c; Figure S12cd, SI).

**In Vivo Sonodynamic and Photothermal Performance of SnNSs@PEG.** Encouraged by the excellent chemotherapy- and PTT-enhanced SDT tri-modal combination therapy in vitro, we further investigated the in vivo antitumor efficacy of SnNSs@PEG-E on H1299 subcutaneous xenograft nude mice. The tumor-bearing mice were randomly divided into 7 groups: 1) saline; 2) NIR + US; 3) free  $\beta$ -elemene (E); 4) SnNSs@PEG-E; 5) SnNSs@PEG-E + US; 6) SnNSs@PEG-E + NIR; 7) SnNSs@PEG-E + NIR + US, in which the tumor regions of group 2, 6, and 7 were exposed to NIR for 10 min ( $1 \text{ W cm}^{-2}$ , 808 nm) and groups 2, 5, and 7 were exposed to US irradiation for 10 min (5 min per cycle, 2 cycles) after the administration of SnNSs@PEG-E. US-triggered ROS generation and NIR-mediated photothermal performance inside the tumors were firstly studied to evaluate the in vivo therapeutic effects of SnNSs@PEG-E. The ROS staining assay indicated that tumor tissue treated by SnNSs@PEG-E + US showed the strongest green fluorescence (Figure 5a; Figure S14, SI) than other control groups (control, SnNSs@PEG-E, and US only), thus demonstrating the efficient ROS generation inside the tumors by the US-triggered SnNSs@PEG-E.<sup>[43,60]</sup> Subsequently, the photothermal performance of SnNSs@PEG-E inside the tumors was measured by an IR thermal camera. The IR thermal images displayed that temperature increase of NIR treatment was only  $3.7 \pm 0.9^\circ\text{C}$ , in contrast, the temperature difference of SnNSs@PEG-E + NIR significantly increased to  $29.8 \pm 1.4^\circ\text{C}$  after 10 min of NIR irradiation (Figure 5bc). The significant temperature increase showed the remarkable photothermal performance of SnNSs@PEG-E inside the tumors during the NIR irradiation. Collectively, the remarkable US-triggered ROS generation and NIR-mediated photothermal performance inside the tumors highlighted the significance of SnNSs@PEG as sonosensitizers and photothermal agents for both SDT and PTT.

**In Vivo Chemotherapy- and PTT-enhanced SDT.** After various treatments, we measured the tumor volumes and body weights of mice every other day over a period of 14 days. Compared with the saline control group, the NIR + US group showed negligible antitumor efficacy. In contrast, a statistically different inhibition of tumor growth was observed for mice treated by free  $\beta$ -elemene and SnNSs@PEG-E, with the tumor growth inhibition ratios of 28%, and 51%, respectively (Figure 5df; Figure S15, SI). The results suggested that SnNSs@PEG could serve as effective anticancer drug delivery carriers for chemotherapy in vivo. Importantly, when the mice were treated by SnNSs@PEG-E with US or NIR exposure, i.e., SnNSs@PEG-E + US, or SnNSs@PEG-E + NIR, the tumor inhibition ratios were 66% and 82%, respectively, higher than that of SnNSs@PEG-E alone (51%, Figure S15,

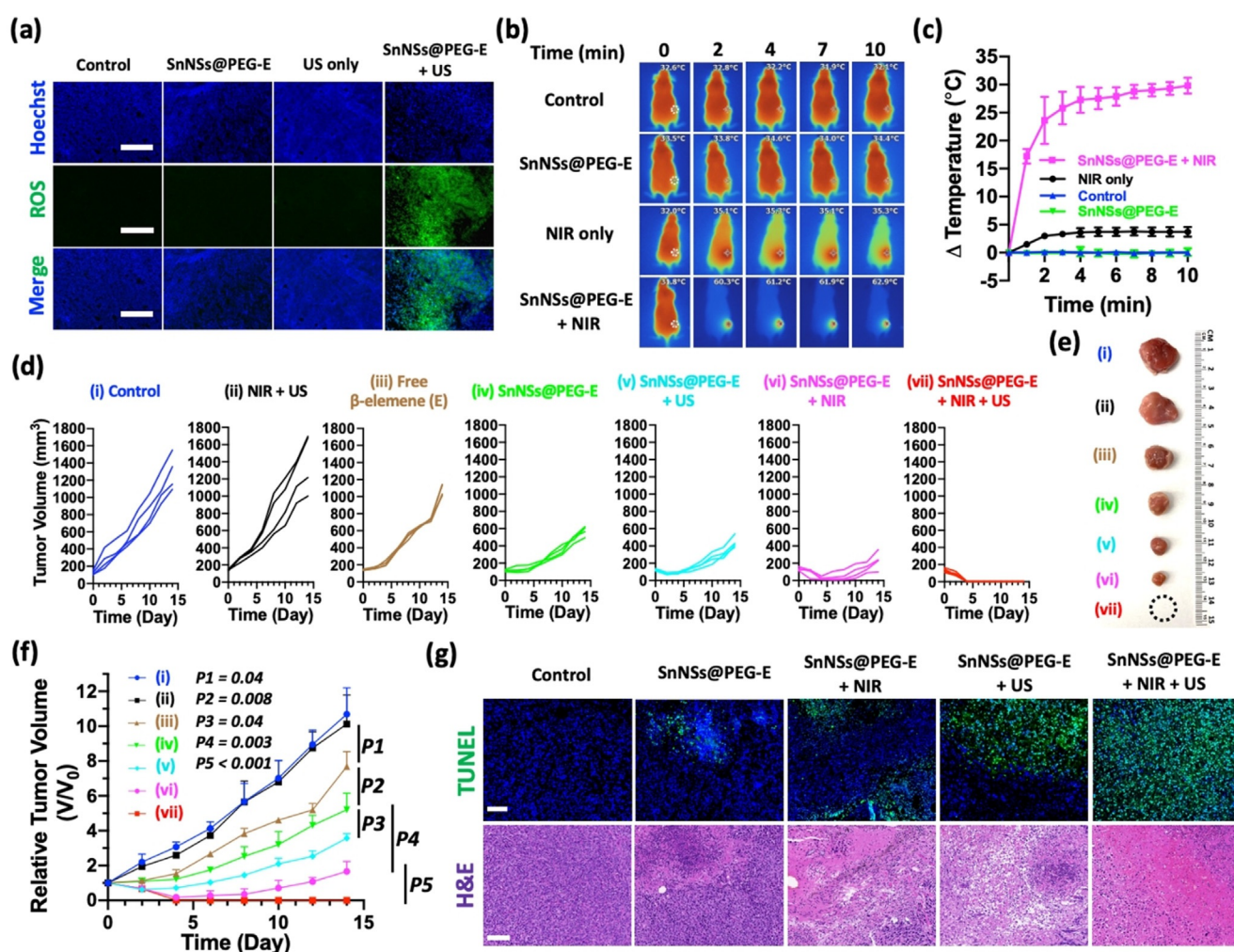


**Figure 5.** In vivo chemotherapy- and PTT-enhanced SDT. a) Fluorescence microscope images of H<sub>2</sub>DCF-DA- and Hoechst-stained tumor slices after various treatments. Scale bars are 100 μm. b) IR thermal images of H1299 tumor-bearing mice after various treatments. The location of the NIR irradiation is indicated by circles (power density: 1 Wcm<sup>-2</sup>). c) Time-dependent temperature increase profiles of tumor regions in (b) after various treatments (*n* = 3). d) Individual and f) average tumor growth curves for 14 days after various treatments (*n* = 4). Data are presented as mean values ± SD. Statistical significance was calculated with a two-tailed Student's *t* test. e) Photo of tumors dissected from the representative mice 14 days after various treatments. g) TUNEL and H&E staining of tumor tissue sections from different treatment groups. Scale bars are 100 μm.

SI). The results demonstrate that, similar to in vitro studies, both chemotherapy-enhanced SDT and chemotherapy-enhanced PTT substantially enhanced the antitumor efficacy and were superior to the chemotherapy alone. It is worth mentioning that the tumor recurrence was observed for both SnNSs@PEG-E + US (on day 4) and SnNSs@PEG-E + NIR (on day 6) (Figure 5df), suggesting the moderate antitumor efficacy of these dual combination therapies and that chemotherapy- and PTT-enhanced SDT tri-modal therapy is required to eliminate the tumors. Remarkably, the tri-modal combination therapy (SnNSs@PEG-E + NIR + US) showed significant inhibition of tumors since the tumors were completely eradicated on day 6 and no recurrence was observed until day 14. The results demonstrated that the chemotherapy- and PTT-enhanced SDT tri-modal combination therapy by SnNSs@PEG-E had an excellent synergistic antitumor efficacy compared with all single and dual combi-

nation therapies, rendering SnNSs@PEG promising nano-platforms for cancer therapeutic applications. Mice were sacrificed on day 14 and the digital photo of the excised tumors (Figure 5e) from the representative mice also reflected the remarkable therapeutic efficacy of the chemotherapy- and PTT-enhanced SDT tri-modal combination therapy. It is worth mentioning that mouse body weight showed no decrease during the therapeutic period (Figure S16, SI), suggesting that no acute toxicities of SnNSs@PEG, NIR, and US irradiation were observed.

Finally, tumor sections were stained with hematoxylin and eosin (H&E) and subjected to terminal deoxynucleotidyl transferase-mediated dUTP-biotin nick end labeling (TUNEL) to approve the therapeutic effect of SnNSs@PEG-E-mediated tri-modal combination therapy (Figure 5g; Figure S17, SI). Consistent with the tumor growth data, tumor treated by chemotherapy- and PTT-enhanced SDT showed

the most severe tissue damage and cell necrosis, supporting that the tri-modal combination therapy effectively eradicated tumors and displayed excellent synergistic antitumor efficacy.

## Conclusion

In summary, for the first time, we have reported a new type of two-dimensional (2D) stanene-based nanosheets (SnNSs) obtained by a liquid-phase exfoliation strategy. Owing to the unique band gap of SnNSs semiconductor (2.3 eV), we applied such SnNSs as sonosensitizers to achieve the ultrasound (US)-triggered generation of  $^1\text{O}_2$  and  $\cdot\text{OH}$  reactive oxygen species (ROS) for sonodynamic therapy (SDT). In addition, we discovered that such black SnNSs could also serve as photothermal agents for near-infrared (NIR)-mediated photothermal therapy (PTT) owing to its excellent photothermal conversion efficiency (37.9%). In vitro studies showed that the therapeutic efficacy of chemotherapy-enhanced SDT and chemotherapy- and PTT-enhanced SDT was significantly enhanced when the cancer cells were treated by  $\beta$ -elemene-loaded SnNSs@PEG followed by the US or NIR and US irradiation. Finally, in vivo studies showed that the chemotherapy- and PTT-enhanced SDT tri-modal combination therapy effectively eradicated tumors and no tumor recurrence was observed 14 days after the treatment. This study not only provides a robust strategy for the large-scale synthesis of 2D stanene-based nanosheets as sonosensitizers for SDT but also establishes general and biocompatible nanoplatforms for tri-modal combination cancer therapy. We also believe that, owing to the unique band gap and physicochemical properties, 2D SnNSs would hold great promises in other fields (e.g., photocatalysis, and energy), beyond nanomedicine.

## Acknowledgements

This work is supported by Harvard Medical School/Brigham and Women's Hospital Department of Anesthesiology-Basic Scientist Grant (No. 2420 BPA075, W.T.), the US METAvivor Early Career Investigator Award (No. 2018A020560, W.T.), and National Natural Science Foundation of China (No. 81730108 and No. 81973635, T.X.). W.T. is a recipient of the Khoury Innovation Award (No. 2020A003219), Stepping Strong Breakthrough Innovator Award (113548), and American Heart Association (AHA) Collaborative Sciences Award (No. 2018A004190). W.T. also received a start-up package (for three years) from the Department of Anesthesiology, Perioperative and Pain Medicine to establish his independent research laboratory at Harvard Medical School and Brigham and Women's Hospital. We thank our department for this generous support.

## Conflict of interest

Prof. Omid C. Farokhzad has financial interests in Selecta Biosciences, Tarveda Therapeutics, XLINK Therapeutics, PrognomIQ, and Seer.

**Keywords:** combination cancer therapy · photothermal therapy · sonodynamic therapy · stanene · two-dimensional materials

- [1] T. J. Dougherty, C. J. Gomer, B. W. Henderson, G. Jori, D. Kessel, M. Korbelik, J. Moan, Q. Peng, *J. Natl. Cancer Inst.* **1998**, *90*, 889.
- [2] D. E. J. G. J. Dolmans, D. Fukumura, R. K. Jain, *Nat. Rev. Cancer* **2003**, *3*, 380.
- [3] C. M. Moore, D. Pendse, M. Emberton, *Nat. Clin. Pract. Urol.* **2009**, *6*, 18.
- [4] X. Qian, Y. Zheng, Y. Chen, *Adv. Mater.* **2016**, *28*, 8097.
- [5] I. Rosenthal, J. Z. Sostaric, P. Riesz, *Ultrason. Sonochem.* **2004**, *11*, 349.
- [6] S. Liang, X. Deng, P. Ma, Z. Cheng, J. Lin, *Adv. Mater.* **2020**, *32*, 2003214.
- [7] J. Ouyang, Z. Tang, N. Farokhzad, N. Kong, N. Y. Kim, C. Feng, S. Blake, Y. Xiao, C. Liu, T. Xie, W. Tao, *Nano Today* **2020**, *35*, 100949.
- [8] F. Gong, L. Cheng, N. Yang, O. Betzer, L. Feng, Q. Zhou, Y. Li, R. Chen, R. Popovtzer, Z. Liu, *Adv. Mater.* **2019**, *31*, 1900730.
- [9] S. Son, J. H. Kim, X. Wang, C. Zhang, S. A. Yoon, J. Shin, A. Sharma, M. H. Lee, L. Cheng, J. Wu, J. S. Kim, *Chem. Soc. Rev.* **2020**, *49*, 3244.
- [10] Y. He, S. Hua Liu, J. Yin, J. Yoon, *Coord. Chem. Rev.* **2020**, *427*, 213601.
- [11] V. G. Deepagan, D. G. You, W. Um, H. Ko, S. Kwon, K. Y. Choi, G. R. Yi, J. Y. Lee, D. S. Lee, K. Kim, I. C. Kwon, J. H. Park, *Nano Lett.* **2016**, *16*, 6257.
- [12] S. Liang, X. Deng, G. Xu, X. Xiao, M. Wang, X. Guo, P. Ma, Z. Cheng, D. Zhang, J. Lin, *Adv. Funct. Mater.* **2020**, *30*, 1908598.
- [13] Y. Liu, Y. Wang, W. Zhen, Y. Wang, S. Zhang, Y. Zhao, S. Song, Z. Wu, H. Zhang, *Biomaterials* **2020**, *251*, 120075.
- [14] K. Ozawa, M. Emori, S. Yamamoto, R. Yukawa, S. Yamamoto, R. Hobar, K. Fujikawa, H. Sakama, I. Matsuda, *J. Phys. Chem. Lett.* **2014**, *5*, 1953.
- [15] W. Tao, N. Kong, X. Ji, Y. Zhang, A. Sharma, J. Ouyang, B. Qi, J. Wang, N. Xie, C. Kang, H. Zhang, O. C. Farokhzad, J. S. Kim, *Chem. Soc. Rev.* **2019**, *48*, 2891.
- [16] A. J. Mannix, Z. Zhang, N. P. Guisinger, B. I. Yakobson, M. C. Hersam, *Nat. Nanotechnol.* **2018**, *13*, 444.
- [17] V. Kochat, A. Samanta, Y. Zhang, S. Bhowmick, P. Manimunda, S. A. S. Asif, A. S. Stender, R. Vajtai, A. K. Singh, C. S. Tiwary, P. M. Ajayan, *Sci. Adv.* **2018**, *4*, e1701373.
- [18] J. Ouyang, C. Feng, X. Ji, L. Li, H. K. Gutti, N. Y. Kim, D. Artzi, A. Xie, N. Kong, Y. N. Liu, G. J. Tearney, X. Sui, W. Tao, O. C. Farokhzad, *Angew. Chem. Int. Ed.* **2019**, *58*, 13405; *Angew. Chem.* **2019**, *131*, 13539.
- [19] G. Le Lay, *Nat. Nanotechnol.* **2015**, *10*, 202.
- [20] A. Molle, C. Grazianetti, L. Tao, D. Taneja, M. H. Alam, D. Akinwande, *Chem. Soc. Rev.* **2018**, *47*, 6370.
- [21] C. Feng, J. Ouyang, Z. Tang, N. Kong, Y. Liu, L. Y. Fu, X. Ji, T. Xie, O. C. Farokhzad, W. Tao, *Matter* **2020**, *3*, 127.
- [22] W. Tao, X. Ji, X. Zhu, L. Li, J. Wang, Y. Zhang, P. E. Saw, W. Li, N. Kong, M. A. Islam, T. Gan, X. Zeng, H. Zhang, M. Mahmoudi, G. J. Tearney, O. C. Farokhzad, *Adv. Mater.* **2018**, *30*, 1802061.
- [23] A. Carvalho, M. Wang, X. Zhu, A. S. Rodin, H. Su, A. H. Castro Neto, *Nat. Rev. Mater.* **2016**, *1*, 16061.
- [24] C. Kamal, M. Ezawa, *Phys. Rev. B.* **2015**, *91*, 085423.

- [25] F. Yang, A. O. Elnabawy, R. Schimmenti, P. Song, J. Wang, Z. Peng, S. Yao, R. Deng, S. Song, Y. Lin, M. Mavrikakis, W. Xu, *Nat. Commun.* **2020**, *11*, 1088.
- [26] J. Ouyang, X. Ji, X. Zhang, C. Feng, Z. Tang, N. Kong, A. Xie, J. Wang, X. Sui, L. Deng, Y. Liu, J. S. Kim, Y. Cao, W. Tao, *Proc. Natl. Acad. Sci. USA* **2020**, *117*, 28667.
- [27] L. Xian, A. P. Paz, E. Bianco, P. M. Ajayan, A. Rubio, *2D Mater.* **2017**, *4*, 041003.
- [28] Y. Wang, G. Qiu, R. Wang, S. Huang, Q. Wang, Y. Liu, Y. Du, W. A. Goddard, M. J. Kim, X. Xu, P. D. Ye, W. Wu, *Nat. Electron.* **2018**, *1*, 228.
- [29] T. Wang, H. Wang, Z. Kou, W. Liang, X. Luo, F. Verpoort, Y. J. Zeng, H. Zhang, *Adv. Funct. Mater.* **2020**, *30*, 2002885.
- [30] F. F. Zhu, W. J. Chen, Y. Xu, C. L. Gao, D. D. Guan, C. H. Liu, D. Qian, S. C. Zhang, J. F. Jia, *Nat. Mater.* **2015**, *14*, 1020.
- [31] J. Deng, B. Xia, X. Ma, H. Chen, H. Shan, X. Zhai, B. Li, A. Zhao, Y. Xu, W. Duan, S. C. Zhang, B. Wang, J. G. Hou, *Nat. Mater.* **2018**, *17*, 1081.
- [32] J. P. Allen, D. O. Scanlon, S. C. Parker, G. W. Watson, *J. Phys. Chem. C* **2011**, *115*, 19916.
- [33] K. Dolabdjian, A. L. Görne, R. Dronskowski, M. Ströbele, H. J. Meyer, *Dalton Trans.* **2018**, *47*, 13378.
- [34] J. Bogdan, J. Pławińska-Czarnak, J. Zarzyńska, *Nanoscale Res. Lett.* **2017**, *12*, 225.
- [35] J. Falson, Y. Xu, M. Liao, Y. Zang, K. Zhu, C. Wang, Z. Zhang, H. Liu, W. Duan, K. He, H. Liu, J. H. Smet, D. Zhang, Q. K. Xue, *Science* **2020**, *367*, 1454.
- [36] B. Wang, J. H. Wang, Q. Liu, H. Huang, M. Chen, K. Li, C. Li, X. F. Yu, P. K. Chu, *Biomaterials* **2014**, *35*, 1954.
- [37] J. T. Robinson, S. M. Tabakman, Y. Liang, H. Wang, H. Sanchez Casalongue, D. Vinh, H. Dai, *J. Am. Chem. Soc.* **2011**, *133*, 6825.
- [38] W. Yin, L. Yan, J. Yu, G. Tian, L. Zhou, X. Zheng, X. Zhang, Y. Yong, J. Li, Z. Gu, Y. Zhao, *ACS Nano* **2014**, *8*, 6922.
- [39] Z. Sun, H. Xie, S. Tang, X. F. Yu, Z. Guo, J. Shao, H. Zhang, H. Huang, H. Wang, P. K. Chu, *Angew. Chem. Int. Ed.* **2015**, *54*, 11526; *Angew. Chem.* **2015**, *127*, 11688.
- [40] K. Hu, L. Xie, Y. Zhang, M. Hanyu, Z. Yang, K. Nagatsu, H. Suzuki, J. Ouyang, X. Ji, J. Wei, H. Xu, O. C. Farokhzad, S. H. Liang, L. Wang, W. Tao, M. R. Zhang, *Nat. Commun.* **2020**, *11*, 2778.
- [41] N. Oehl, G. Schmuelling, M. Knipper, R. Kloepsch, T. Placke, J. Kolny-Olesiak, T. Plaggenborg, M. Winter, J. Parisi, *CrystEngComm* **2015**, *17*, 8500.
- [42] P. Carloni, E. Damiani, L. Greci, P. Stipa, F. Tanfani, E. Tartaglioni, M. Wozniak, *Res. Chem. Intermed.* **1993**, *19*, 395.
- [43] X. Wang, X. Zhong, L. Bai, J. Xu, F. Gong, Z. Dong, Z. Yang, Z. Zeng, Z. Liu, L. Cheng, *J. Am. Chem. Soc.* **2020**, *142*, 6527.
- [44] P. Zhu, Y. Chen, J. Shi, *ACS Nano* **2018**, *12*, 3780.
- [45] P. Huang, X. Qian, Y. Chen, L. Yu, H. Lin, L. Wang, Y. Zhu, J. Shi, *J. Am. Chem. Soc.* **2017**, *139*, 1275.
- [46] M. Ochsner, *J. Photochem. Photobiol. B* **1997**, *39*, 1.
- [47] X. Han, J. Huang, X. Jing, D. Yang, H. Lin, Z. Wang, P. Li, Y. Chen, *ACS Nano* **2018**, *12*, 4545.
- [48] Y. Harada, K. Ogawa, Y. Irie, H. Endo, L. B. Feril, T. Uemura, K. Tachibana, *J. Controlled Release* **2011**, *149*, 190.
- [49] F. Gong, L. Cheng, N. Yang, Y. Gong, Y. Ni, S. Bai, X. Wang, M. Chen, Q. Chen, Z. Liu, *Nat. Commun.* **2020**, *11*, 3712.
- [50] C. M. Hessel, V. P. Pattani, M. Rasch, M. G. Panthani, B. Koo, J. W. Tunnell, B. A. Korgel, *Nano Lett.* **2011**, *11*, 2560.
- [51] H. Xie, Z. Li, Z. Sun, J. Shao, X. F. Yu, Z. Guo, J. Wang, Q. Xiao, H. Wang, Q. Q. Wang, H. Zhang, P. K. Chu, *Small* **2016**, *12*, 4136.
- [52] R. Kurapati, K. Kostarelos, M. Prato, A. Bianco, *Adv. Mater.* **2016**, *28*, 6052.
- [53] W. Tao, X. Zhu, X. Yu, X. Zeng, Q. Xiao, X. Zhang, X. Ji, X. Wang, J. Shi, H. Zhang, L. Mei, *Adv. Mater.* **2017**, *29*, 1603276.
- [54] W. Yue, L. Chen, L. Yu, B. Zhou, H. Yin, W. Ren, C. Liu, L. Guo, Y. Zhang, L. Sun, K. Zhang, H. Xu, Y. Chen, *Nat. Commun.* **2019**, *10*, 2025.
- [55] X. Pan, W. Wang, Z. Huang, S. Liu, J. Guo, F. Zhang, H. Yuan, X. Li, F. Liu, H. Liu, *Angew. Chem. Int. Ed.* **2020**, *59*, 13557; *Angew. Chem.* **2020**, *132*, 13659.
- [56] W. Chen, C. A. Glackin, M. A. Horwitz, J. I. Zink, *Acc. Chem. Res.* **2019**, *52*, 1531.
- [57] C. A. Cheng, W. Chen, L. Zhang, H. H. Wu, J. I. Zink, *J. Am. Chem. Soc.* **2019**, *141*, 17670.
- [58] C. A. Cheng, W. Chen, L. Zhang, H. H. Wu, J. I. Zink, *Chem. Commun.* **2020**, *56*, 10297.
- [59] X. Ji, Y. Kang, J. Ouyang, Y. Chen, D. Artzi, X. Zeng, Y. Xiao, C. Feng, B. Qi, N. Y. Kim, P. E. Saw, N. Kong, O. C. Farokhzad, W. Tao, *Adv. Sci.* **2019**, *6*, 1901211.
- [60] X. Zhong, X. Wang, L. Cheng, Y. Tang, G. Zhan, F. Gong, R. Zhang, J. Hu, Z. Liu, X. Yang, *Adv. Funct. Mater.* **2020**, *30*, 1907954.

Manuscript received: December 8, 2020

Accepted manuscript online: January 12, 2021

Version of record online: February 18, 2021